A Comprehensive Solution for Simulating Ultra-Shallow Junctions: From High Dose/Low Energy Implant to Diffusion Annealing

Introduction

The persistent semiconductor technology trend of shrinking down device size requires development of veryaggressive technological setups consisting in high dose/low energy implants, followed by rapid thermal anneals (RTA). Since it is now well established that phenomena involved in ion implantation will play a key role intransient enhanced diffusion (TED), advanced process simulation tools need to model accurately these two steps for deep submicron CMOS technologies. This paper presents the comprehensive solution fully integrated into the commercial SILVACO TCAD suite needed by advanced process technology designers. The implantation step simulated with a Monte-Carlo code based on the Binary Collision Approximation (BCA), provides initial impurity and defects profiles. The diffusion simulation includes the latest physical model developments: dopantdefect pair, interstitials or vacancy clusters and mixed dopant-defect clusters formation and evolution. Although the complete model covers a wide range of physical interactions, it is straightforwardly usable thanks to a comprehensive set of parameters obtained using an original calibration methodology.

Implant and Diffusion Models

Ion implantation and radiation damage are modelled by means of a simulation technique based on the BCA. The principal assumption of this approximation is that the interaction of energetic particles may be separated into a series of two-body encounters. The real benefit of this approach is the moderate speed of calculation combined with the possibility of including single crystal structures in the calculation. The slowing down of energetic particles is a result of nuclear and electronic stopping. An universal Ziegler-Biersack-Littmark (ZBL) screening function is used for the interatomic potentials while the electron stopping is modelled through *local* and *non-local* contributions to the inelastic energy losses. The *non-local* is that of Wang, *et al.* [1], and the local stopping is calculated using the technique of Azziz, et al. [2], with a correction for high energies when energy transfer diminishes as described in [3].

In order to simulate the radiation induced damage the model accounts for all collision events within the collision cascade. As demonstrated elsewhere [4], up to 80% of the created I-V pairs can annihilate due to recombination, so the local arrangement of the displaced atoms and vacancies, from where these atoms originated, becomes important when spontaneous recombination has to be taken into consideration. Furthermore, it is not only the number of defects but also their initial spatial distribution, which influences the residual damage. This pertains especially to rearrangement of defects (formation of clusters, loops, voids, etc.) before subsequent migration and thermal annealing is precluded. As a first approach to the initial distribution of defects, at the completion of the cascade, the model of Snyder and Neufeld [5] is used. The value of the vacancy capture radius was carefully chosen so that the amount of residual damage is comparable to that calculated with other techniques, e.g. Kinetic Monte-Carlo.

The full advanced diffusion model will use as initial input, the impurity and defects profiles calculated previously with the BCA code. This model is made of three separated parts, each one corresponding to one particular phenomenon, dynamically interacting with each other [6].

The Classical Dopant Diffusion model [7] takes into account all the known couplings existing between the dopant and point defects (Self interstitials and Vacancies). All the charge states experimentally established for both the point defects and dopant/defects pairs are considered. The local equilibrium is
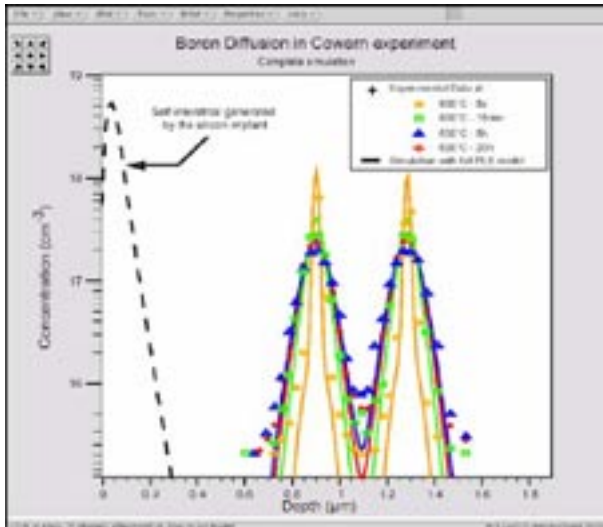

INSIDE

SILVACO INTERNATIONAL

Figure 1. Simulation (solid line) of Cowern experiment (symbols) [12] where two boron MBE-pics diffuse after a Si implantation at 40keV/ 2.10^{13} cm^{-3}. During the annealing, interstitial clusters will evaluate following through an Ostwald ripening scheme and will control the acceleration of the dopant diffusion.
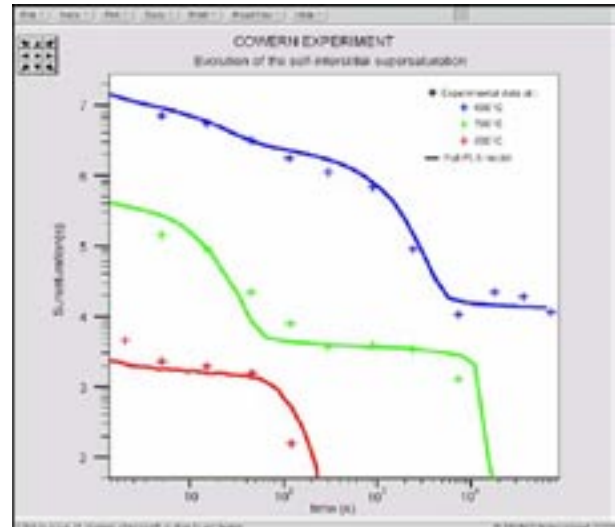

Figure 2. Comparison between experimental (symbols) and calculated (solid line) I supersaturation evolution in Cowern experiment [12]. The good agreement between experiment data and simulations prove that the new model is able to handle all defects interactions and to simulate the various regimes in the dopant diffusion acceleration.

not assumed for the various formation/dissociation reactions, thus the full system of continuity equations for both dopant, point defect and clusters is dynamically solved. Moreover, a model has been implemented for dopant precipitation when the solid solubility limit is reached.

The second component of the model deals with defect clustering effects where some of residual excess point defects nucleate and evolve into various forms of interstitial clusters (IC) like {311} defects, dislocation loops or vacancy clusters (VC). This evolution is explained by a competitive growth and dissolution of interstitial or vacancy clusters. These phenomena are described by the Ostwald ripening

theory based on the reduction of free energy per defect of the extended defect which leads to the growth in size of the clusters during annealing [8] [9]. This phenomenon drives the interstitial super saturation and therefore modifies the dopant diffusion and clustering behavior.

Eventually, another part of excess point defects will be trapped by dopant atoms, to form immobile complexes, which makes up the third part of the model. In case of boron implantation, the model takes into account the formation of Boron Interstitial Clusters (BIC), like BI_2^+, B_2I^0, $B_3I_2 + B_4I_3 +$, where charge states are also considered according to [10]. While in the case of arsenic implantation, As atoms aggregate preferentiall with vacancies to form
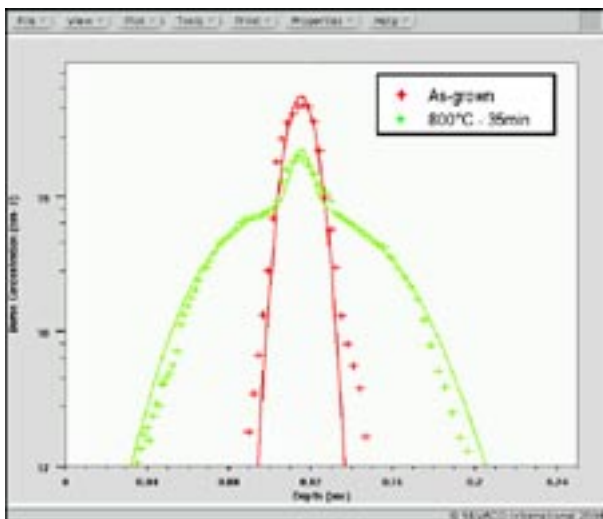

Figure 3. Comparison between experimental (symbols) and simulated (solid line) B profiles evidencing the influence of BIC's. Data are extrated from Pelaz *et al.* (1997) [13].
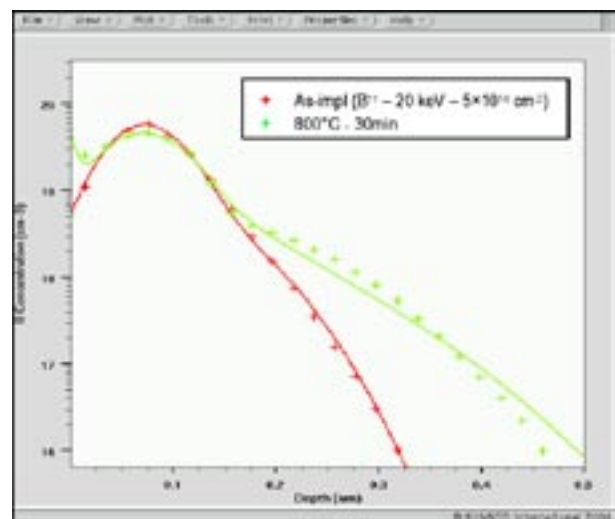

Figure 4. Comparison between experimental (symbols) [14] and simulated (solid line) B profiles implanted at 20 keV/2.10^{14}cm^{-2}, annealed at 800°C for 30 min. At high concentration, boron stay inactive due to the formation of Boron Interstitial Clusters (BICs).
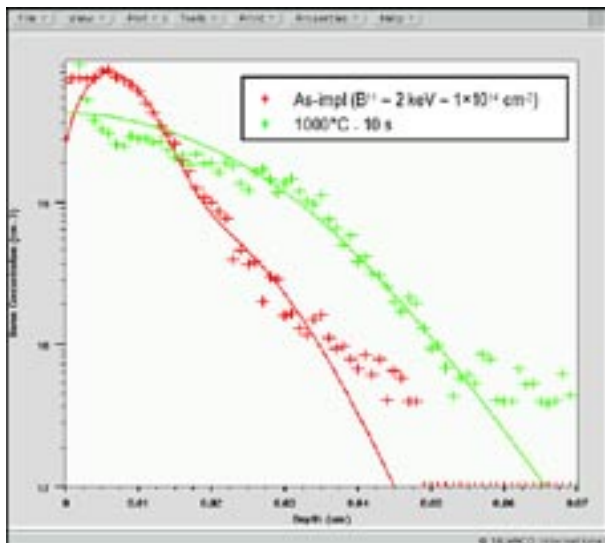
Figure 5. Simulation of ultra low energy implantation of B followed by RTA. (see ref. [15]). (Experimental data are represented with various symbols; lines are the simulation results).

Figure 6. Simulation of an ultra low energy implantation of As followed by spike annealing. (see ref. [16]). (Experimental data are represented with various symbols; lines are the simulation results).

As2V0 or As4V0 complexes. This clustering phenomenon leads to an unwanted inactivation and immobilization of the implanted species.

Moreover, this simulation tool is flexible and expandable since other phenomena which may affect the dopant diffusion, i.e. the presence of carbon or fluorine atoms, can be easily incorporated by simply adding new chemical reaction and its coefficients to the model file. The use of such a complex physically based model involves many parameters which can be accurately determined only by a calibration methodology presented hereafter.
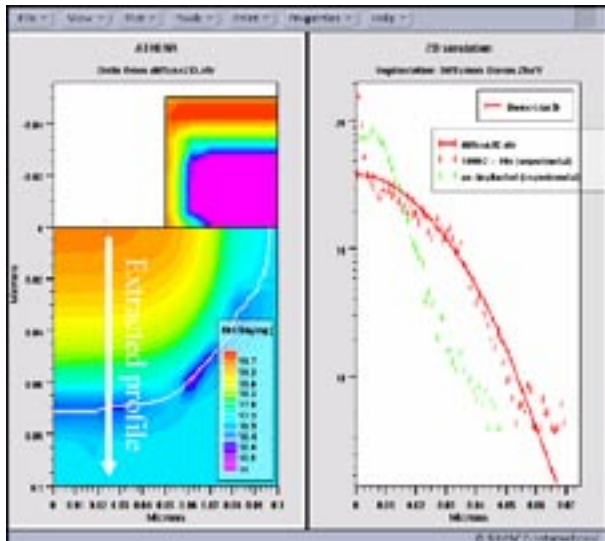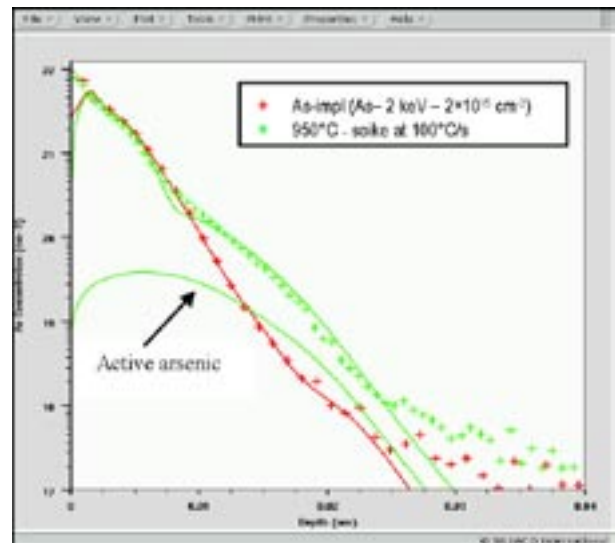
Calibration Methodology

The diffusion model presented above has up to 40 physical parameters including formation energies, kinetic coefficients, etc. Having in mind to keep them physically significant, an original calibration methodology has been developed [11]. It is based on specific statistical strategies, which include screening and sorting of relevant parameters, Design of Experiments (DoE) and Responses Surface Models (RSM) optimizations. This has been applied sequentially to all three components of the diffusion model. This calibration methodology has been successfully used on a broad range of experiments. Relevant simulations are presented below.
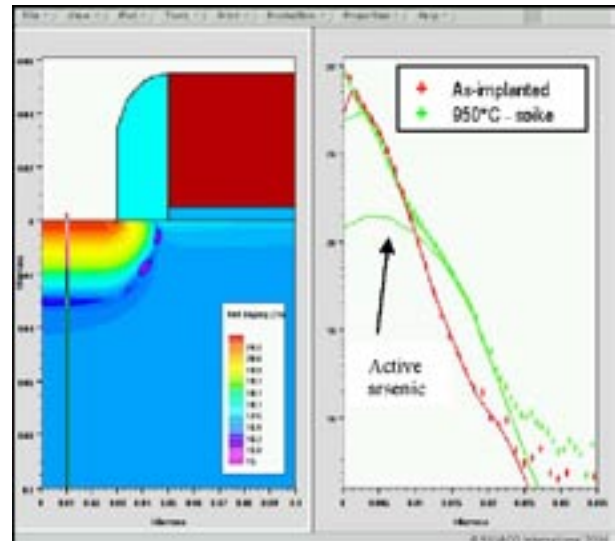

Figure 7. Simulation of boron 2D distribution implanted at 2 keV/10^{14}cm^{-2} and annealed at 950oC for 10 sec. Comparison between experimental data (symbols) (extracted from [15]) and profile extracted from the 2D simulation (solid line) evidences the quality of the new diffusion model.

Figure 8. 2D simulation of arsenic diffusion implanted at 2 keV/5.10^{14}cm^{-2} and spike annealed at 1000oC with a ramp up estimated at 100oC/s. Most of the arsenic precipitate and stay inactive above solid solubility limit. (Experimental data are extracted from [16]).
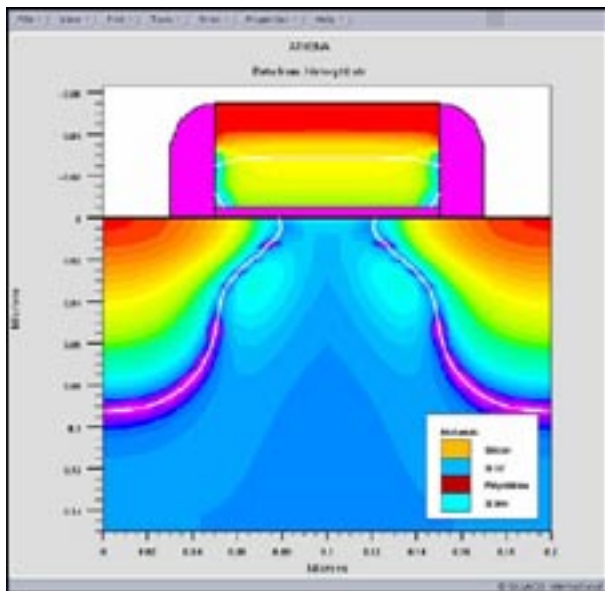
Figure 9. 2D simulation of P-MOS transistor with boron diffusion after a low energy implant and RTA and with the presence of arsenic halo.
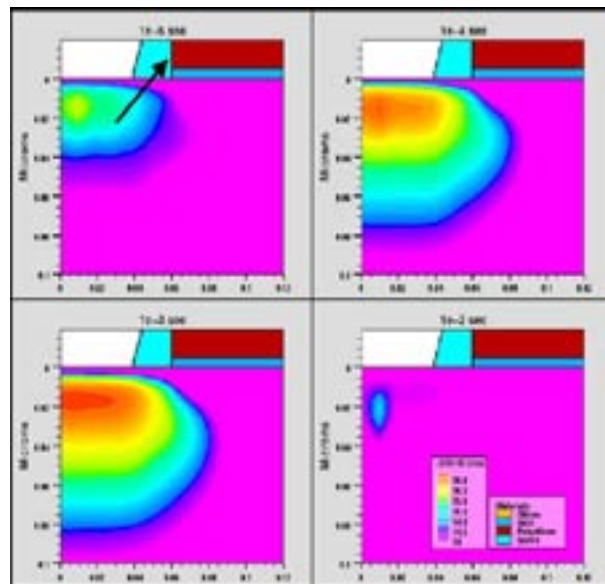

Figure 10. Evolution in time of the <311> defects concentration where at the early stage of the annealing they grow by exchange their interstitials to form clusters and finally dissolve according to the Ostwald ripening theory.

Simulation Results

A complete set of simulations has been performed using both BCA implant and advanced diffusion models. First, the interstitial clusters part of the model has been validated using the experimental data obtained by Cowern *et al.* [12] (Figures 1 and 2). Briefly, this experiment consists in observing the diffusivity of two boron marker layers after a silicon implantation at 40 keV to a dose of 2.10^{13}at.cm^{-2}. As exhibited in figure 1b, the model accurately predicts the two stages of the diffusion acceleration: the first plateau appearing at the earliest stage of the annealing, governed by the formation of small interstitial clusters, the second one characteristic of the competitive growth of {311} defects. Secondly, the calibration procedure was applied to tuning of the Pelaz experiment [13] in which a buried boron layer with a peak concentration above the 1019cm-3 level is annealed at 800°C for 35 min in the presence of defects created by a 2.10^{13}cm^{-2} Silicon implant. It can be seen in Figure 3 that substantial portion of boron concentration may be kept immobile and inactive even below the solid solubility level, because boron atoms are trapped in mixed clusters (Boron Interstitial Clusters). The two previous experiments were used to calibrate the diffusion model, while its verification was carried out by characteristic implant/diffusion steps used in advanced technologies.

As a validation test of the ability of our diffusion model to handle all the interactions existing during the dopant diffusion, three most representative implantation/diffusion experiments were chosen for simulations. The first experiment presented in figure 4 shows that in the case of medium dose 20 keV boron implant annealed for 30 min at 800°C [14] most of the dopant concentration stays immo-

bile because of the BICs formation. Moreover, the model provides a very important technological insight about the dopant inactivation, since a substantial portion of boron remains inactive. The last two examples presented in figures 5 and 6, simulate very low energy implant steps at 2 keV, respectively for boron [15] and arsenic [16], followed by a typical modern rapid thermal annealing (RTA) step. Complexity of these two simulations lies in the steepness of the implanted dopant concentration and the vicinity of the surface, where recombination phenomenon occurs. Unlike the boron experiment, where most of the dopant is active after the annealing, in the case of the arsenic the solid solubility model seriously affects both the shape of diffused profile and its inactive portion.

The two last simulations (Figures 5 and 6) have been performed in 2D then compared to experimental data [15][16]. Finally a complete NMOS transistor has been fully simulated in 2D (Figure 7). During the annealing step, evolution and distribution of the <311> defect can be monitored (Figure 8) in order to better understand and thus optimize the dopant diffusion acceleration by defect engineering.

All the coupled equations of the model are solved in a new specific solver called Difsim. One of the particularities of this solver is that it is able to integrate quickly new equations just by adding new reactions in the model files. Since this solver has been particularly optimized for this model, simulation times are short. For instance, it has only taken less than 7 min on a 2GHz-LinuxPC to simulate the 2D simulation of Figure 9.

Simulating the Device Characteristics of MEH-PPV Polymer Light Emitting Diodes Using *ATLAS*

Introduction

Organic light emitting diodes (OLEDs) are attracting great interest in the display technology industry due to their promising low cost large area manufacturing and relative ease of fabrication using low processing temperatures. Although the research work of OLEDs has began since early 1980 and has been well established, there is still no commercially available software that can simulate the electrical and optical behavior of these organic polymer/monomer based devices. As such, Silvaco-*ATLAS* has recently extended its capability to simulate these devices using a variety of appropriate organic polymer/monomer models.

In this article, we will present the use of *ATLAS* in simulating OLEDs based upon the commonly used organic material i.e. MEH-PPV [more fully known as poly(2-methoxy,5-(2′-ethyl-hexoxy)-1,4-phenylenevinylene)]. MEH-PPV has been chosen in the paper since it has been an attractive material in OLED fabrication because of its solubility in common organic solvents, in conjunction with a low operating voltage for light emission and relatively high conversion efficiency [1].

Device Simulation Structure

Figure 1 shows the simulation structure used in this paper. It is a three layer device; typically consisting of the MEH-PPV polymer film sandwiched between an Indium-Tin-Oxide (ITO) coated glass substrate and a metal. The ITO is the anode while the cathode is made up of metal. Whether these contacts are electron or hole injection limited depends on their workfunction with respect to the LUMO and HOMO energy levels of the MEH-PPV.
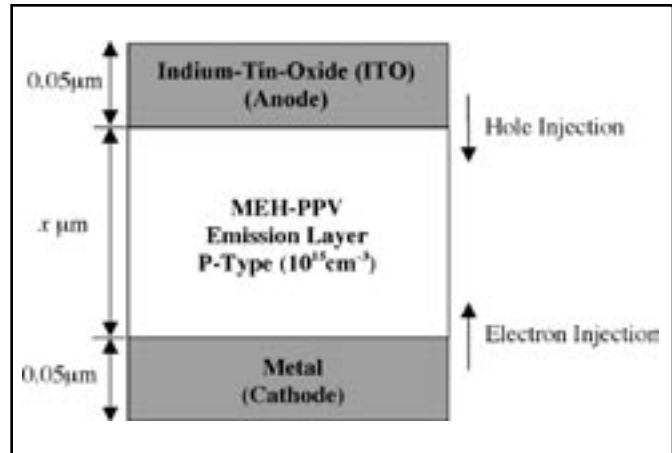

Figure 1 Schematic diagram of the simulation structure.

In this simulation, the thickness of both electrodes are set to 0.05μm while the thickness of the MEH-PPV will be varied between the range of 475Å to 2100Å so as to study the electrical characteristics of the OLED device.

Models and Device Parameters

In this organic polymer LED simulation, the Poole-Frenkel-like mobility model and the Langevin bimolecular recombination model have been used as the transport and recombination mechanism. These models are enabled in ATLAS by specifying the parameters PFMOB and LANGEVIN in the MODEL statement. In addition, to infer the radiative rates for luminescence or phosphorescence due to the Langevin recombination in organic polymer LEDs, the distribution of singlet or triplet excitons has to be calculated. *ATLAS* has included the exciton rate equation which is self-consistently solved along with the electron and hole drift diffusion equations. To enable the self-consistent simulation of excitons, the EXCITON parameter was also included in the MODEL statement.

For the Poole-Frenkel-like mobility model, additional parameters such as the DELTAEN.PFMOB, DELTAEP.PFMOB, BETAN.PFMOB and BETAP.PFMOB, are specified in the MOBILITY statement. DELTAEN.PFMOB and DELTAEP.PFMOB are the thermal activation energy of the organic polymer at zero electric field for electrons and holes respectively while BETAN.PFMOB and BETAP.PFMOB are the electron and hole Poole-Frenkel factor respectively. The device material parameters used in this simulation are given in Table 1

Parameter	Magnitude	Units
Bandgap energy, E_g	2.1	eV
Temperature, T	300	K
Affinity	2.8	eV
ITO Workfunction	4.7	eV
Density of State, N_0	2.5×10^{19}	cm^{-3}
Hole mobility, μ_p	0.5×10^{-4}	$cm^2 V^{-1} s^{-1}$
Electron mobility, μ_n	0.5×10^{-5}	$cm^2 V^{-1} s^{-1}$
Exciton lifetime, τ	1×10^{-9}	s
Exciton diffusion length, L_D	1×10^{-6}	cm
Fraction of excitons formed as singlets, F	0.45	unitless
Relative permittivity, ε_r	3.0	unitless
Richardson constant	120	$A cm^{-2} K^{-2}$

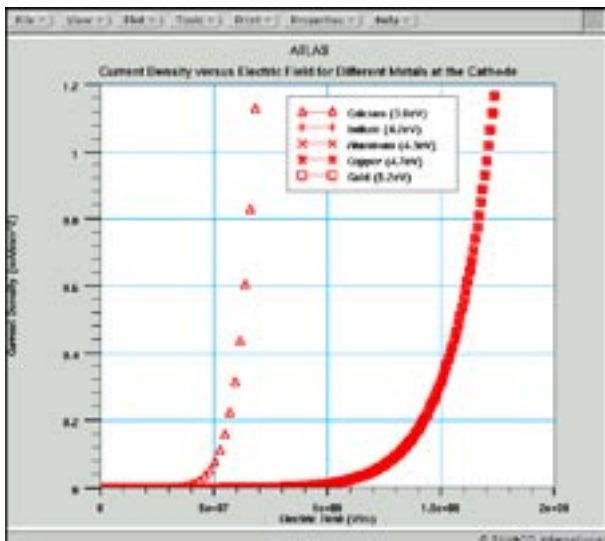Table 1. Device parameters used in this simulation.

Figure 2 Simulated current density versus electric field characteristics of 1200Å OLED device with different metals ranging from calcium to gold.

Results

In this paper, we will simulate both the single-carrier "hole-only" and "electron only" and also the two-carriers OLED devices. The simulation results will then be compared to the experimental results mentioned as in [2].

The "hole-only" device can be obtained by using a high workfunction metal such as In (4.2eV), Al(4.4.eV), Ag(4.6eV), Cu(4.7eV) or Au(5.2eV) at the cathode. The use of high workfunction metal contributes a high energy offset between the fermi energy at the cathode and the LUMO level in the MEH-PPV (which is 2.8eV). This effectively reduces the number of injected electrons at the cathode and therefore the injected holes at the anode dominate. Figure 2 shows the current density versus

electric field characteristics of a 1200Å thick OLED device with different metals. As can be seen from the graph, despite the fact that the workfunction of the cathode varies by more than 1eV between indium and gold, the simulated curves are identical, indicating that the electron injecting plays no part in determining the device characteristics.

Next, we will study the electrical characteristics of the "hole-only" ITO/MEH-PPV/Cu device by varying its polymer thickness. Figure 3a shows the simulated current density versus the applied voltage of the "hole-only" polymer device with different polymer thickness ranging from 475Å to 2100Å. It is clear from this graph that increasing the polymer thickness increases the operating voltage of the device. On the other hand, figure 4a shows a plot of the current density versus the electric field. From this graph, it can be seen that the current density remains almost the same at a specific electric field irregardless of the thickness of the polymer device. This reveals that the I-V characteristics of the "hole-only" devices are dependent on the electric field strength and not the applied voltage. This is in good agreement with the experimental results obtained in [2] (which are reproduced in Figure 3b and 4b).

A similar analysis was carried out for the "electron-only" devices. Here, the ITO at the anode contact is replaced with a lower workfunction metal such as Nd (3.2eV) or Mg (3.7eV). Due to the large energy offset between the fermi level of the anode and the HOMO of the MEH-PPV, the number of injected holes are significantly reduced. As such, most of the carriers in such devices are almost dominated by electrons. Figure 5a shows a plot of the simulated current density versus electric field for an "electron-only" Nd/MEH-PPV/Ca device with vary-
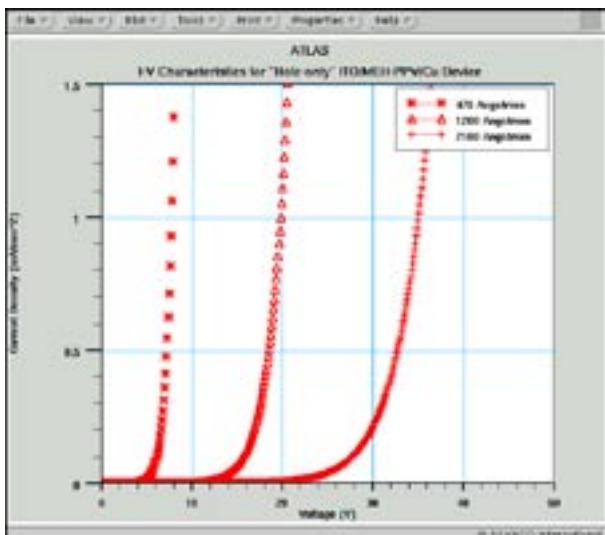

Figure 3a Simulated I-V characteristics of "hole-only" ITO/ MEH-PPV/Cu device for different polymer thickness.
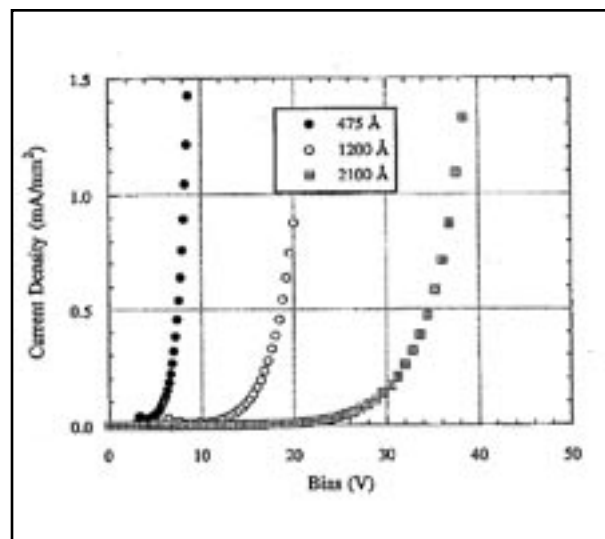

Figure 3b Experimental I-V characteristics of "hole-only" ITO/ MEH-PPV/Cu device obtained from figure 4a of [2].
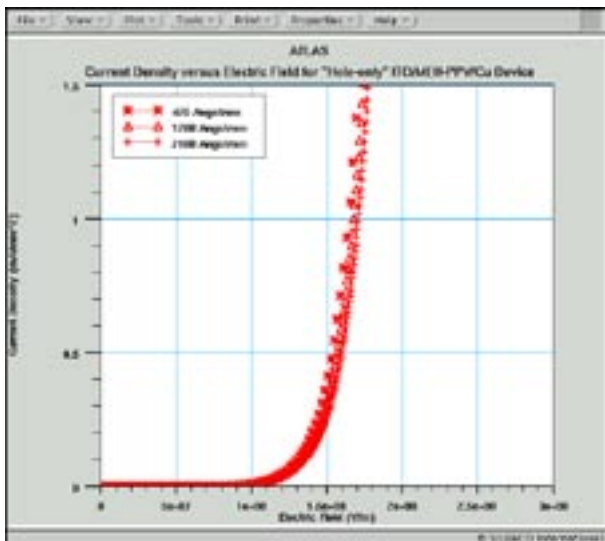
Figure 4a Simulated current density versus electric field of "hole-only" ITO/MEH-PPV/Cu device for different polymer thickness.
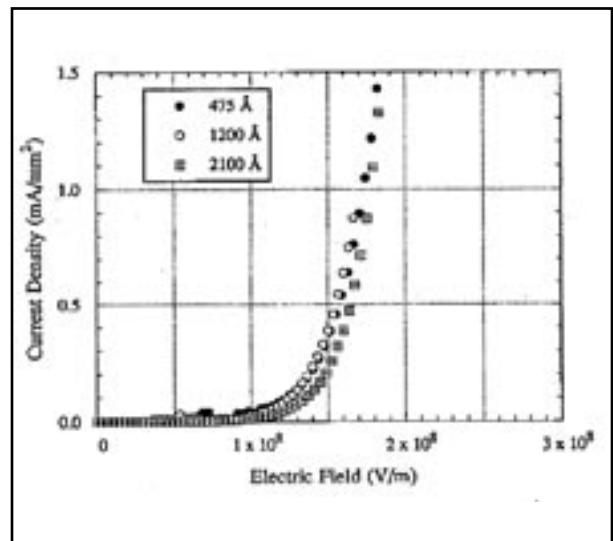

Figure 4b Experimental current density versus electric field of "hole-only" ITO/MEH-PPV/Cu device obtained from figure 4b of [2].

ing polymer thickness of 1200Å, 1500Å and 2100Å. The experimental results are as shown in figure 5b.

From the graphs, it can be seen that both the simulated and measured results agree well. Both graphs show similar field-dependent behavior with significant current density starting at electric field of around 1.3×10^8 V/m. Therefore, the electrical characteristics of the "electron-only" devices are also electric field dependent, just like the "hole-only" devices.

Finally, we will study the electrical characteristics of the two-carriers ITO/MEH-PPV/Ca OLED device. The work-function of the calcium used here is 2.9eV. Figure 6a and

6b shows the simulated and experimental current density versus electric field characteristics of the two-carriers OLED device with four different polymer thicknesses ranging from 475Å to 2100Å respectively.

Once again, both simulated and experimental results of the two-carriers ITO/MEH-PPV/Ca device agree well and they showed that the current density curves are almost similar for different polymer thickness. Both plots also reveals the operating field of the two-carriers OLED device to be at around 4×10^7 V/m. This is very much lower than that of single-carrier "hole-only" or "electron-only" OLED devices.
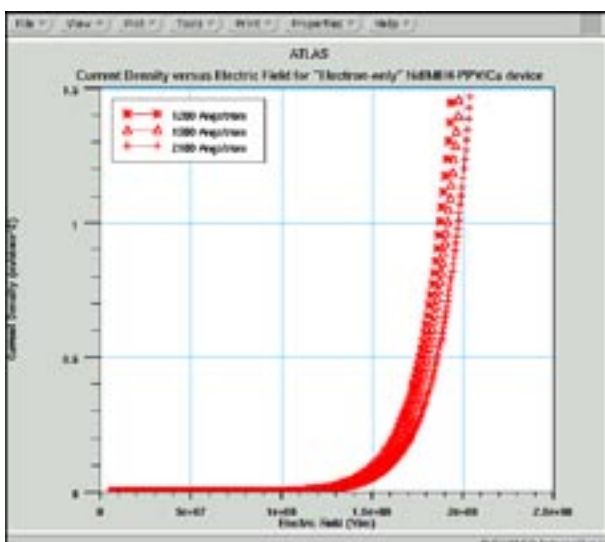

Figure 5a Simulated current density versus electric field of "electron-only" Nd/MEH-PPV/Ca device for different polymer thickness.
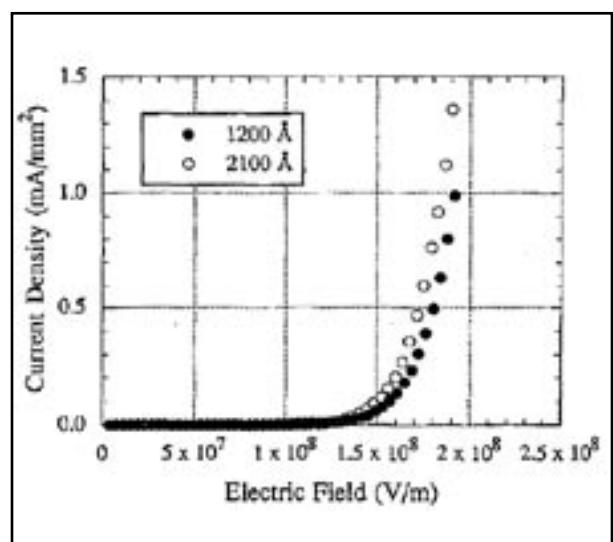

Figure 5b Experimental current density versus electric field of "electron-only" Nd/MEH-PPV/Ca device obtained from figure 8 of [1].
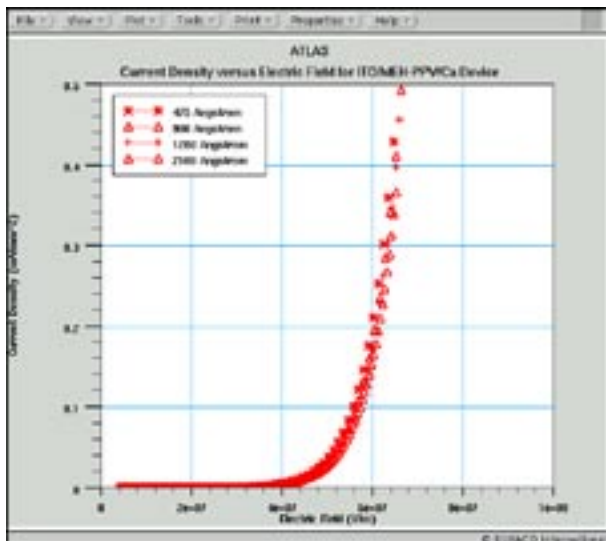
Figure 6a Simulated current density versus electric field characteristics of ITO/MEH-PPV/Ca device for different polymer thickness.
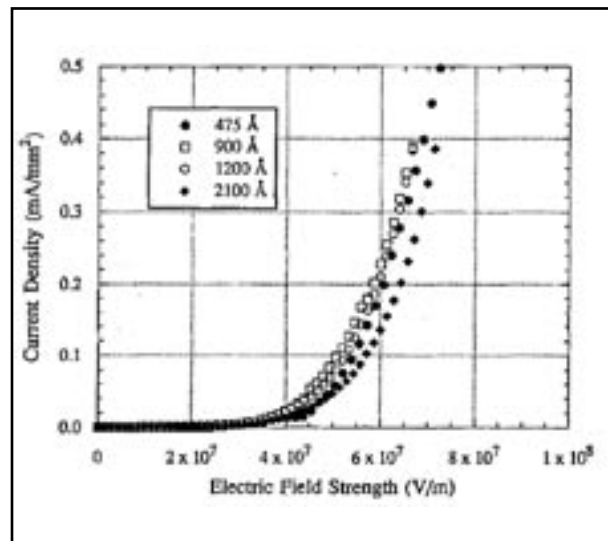

Figure 6b Experimental current density versus electric field of ITO/MEH-PPV/Ca device for different polymer thickness obtained from figure 2b of [1].

Conclusion

The newly implemented organic polymer/monomer module into *ATLAS* has accurately simulated the experimental I-V characteristics of the MEH-PPV OLED devices. It has been shown that by varying the polymer thickness, *ATLAS* is able to simulate the current density of the polymer devices with great accuracy. In addition, the simulated current density versus electric field plots coincided with the experimental plots. Both results suggest that the electric field strength rather than the operating voltage determines the device characteristics of the OLED devices. Therefore, the easiest way to control the operating voltage of the OLED devices is by changing the polymer thickness.

References

1. F. Wudl, P. M. Allemand, G. Srdanov, Z. Ni, and D. McBranch, in Materials for Nonlinear Optics: Chemical Perspectives, edited by S. R. Marder, J. E. Sohn, and G.D. Stucky, American Chemical Society Symposium Series, Vol. 455, pp. 683-686.

2. I. D. Parker, " Carrier tunneling and device characteristics in polymer light-emitting diodes", J. Appl. Phys. 75, pp. 1656-1666.

Conclusion

All the presented physical phenomena are successfully simulated with the BCA implantation module and with the new advanced diffusion model implemented within the SILVACO's framework. A global and original calibration methodology has been used to provide the model with a physical set of parameters which allows to successfully simulate a very broad range of experimental setups, from low to high energy and dose implants followed by anneals ranging from a few seconds to tens of minutes. These results demonstrate that the simulation needs for key process steps of current technologies are fulfilled.

Acknowledgment

References

[1] Wang, *et al.*, Phys. Rev. A44, p.1768, (1991).

[2] Azziz, *et al.*, Physica Status Solidi 142, p. 35, (1987).

[3] Dort, et al., Solid-State Electronics 37, p.411, (1994).

[4] R. Smith Editor, *Atomic and Ion Collisions in Solids and at Surfaces*, Cambridge Univ. Press, (1997).

[5] Snyder and Neufeld, Phys. Rev. 97, p.1636, (1955).

[6] F. Boucard Ph.D. thesis (2003).

[7] Mathiot *et al.*, J. Appl. Phys. 55, p. 3518.(1984).

[8] Claverie *et al.* Nucl. Instr. Meth. B 147, p.1 (1999).

[9] Ortiz et al., *MRS Symp* 669, p 5.6 (2001).

[10] Lenosky *et al.*, Appl. Phys. Lett., 77, p.1834, (2000).

[11] F. Roger Ph.D. thesis (2002).

[12] Cowern *et al.* Phys. Rev. Lett. 82, p. 4460, (1999).

[13] Pelaz *et al.*, Appl. Phys. Lett., 70, p. 2285, (1997).

[14] Solmi *et al.* J. Appl. Phys. , 88, p. 2135, (1991).

[15] B. Colombeau Ph. D. Thesis (2001).

[16] P. Fastenko Ph. D. Thesis (2002).

Calendar of Events

May

1
2
3
4
5
6
7
8   Nanotech - Anahiem, CA
9   Nanotech - Anahiem, CA
10 Nanotech - Anahiem, CA
11 Nanotech - Anahiem, CA
12 Nanotech - Anahiem, CA
13
14
15
16
17
18
19
20
21
22
23 ISPSD – Santa Barbara, CA
24 ISPSD – Santa Barbara, CA
25 ISPSD – Santa Barbara, CA
26 ISPSD – Santa Barbara, CA
27
28
29
30
31

June

1
2
3
4
5
6
7
8
9
10
11
12
13 DAC - Anahiem, CA
14 DAC - Anahiem, CA
15 DAC - Anahiem, CA
16 DAC - Anahiem, CA
17 DAC - Anahiem, CA
18
19
20
21
22
23
24
25
26
27
28
29
30

Bulletin Board

DAC – Design Automation Conference (DAC)

Come and see Silvaco at the largest annual EDA conference in booth #1006 across the street from Disneyland. Our best applications engineers will be on hand to demonstrate our latest software products to solve your IC design automation problems.

International Symposium on Power Semiconductor Devices (ISPD)

Silvaco is a world leader in the infrastructure for power semiconductor devices. Our process and device simulation software is critical for R&D in the fab. Our PDK-driven High-Voltage Custom IC Design Flow goes from schematic capture, to simulation, layout, physical verification and parasitic extraction. The Silvaco tool flow is supported by leading power management process foundries

2005 NSTI Nanotechnology Conference (NanoTech)

Leading nanotechnology companies use Silvaco IC design tools MEMS design and layout. Silvaco is also presenting a paper on the results of the next generation compact model candidate HiSIM-RF that Silvaco is sponsoring with the Compact Modeling Council.

*If you would like more information or to register for one of our our workshops, please check our web site at **http://www.silvaco.com***

Hints, Tips and Solutions

Robin Jones, Sr. Applications Engineer

Q. I am currently using *ATLAS/ Blaze* to model the electrical properties of an LED device that I am investigating. Is it possible to examine the reverse ray trace from my simulated structure so that I can examine the angular distribution properties of the optical output of the device?

A. *ATLAS* enables users to perform a reverse ray trace on their LED device allowing the calculation of the optical coupling efficiency of LED/OLED devices. The optical coupling efficiency is defined as the portion of the luminous power that exits the device. The reverse ray tracing algorithm is performed on a structure file containing previously simulated electrical / optical characteristics of the device in question. To perform a reverse ray trace on the device use is made of the save statement. An example of the *ATLAS* syntax for a reverse ray trace is given as the following:

```
save fast angpower=angle1_
fast.log rayplot=ray_angle1_
fast.log x=2.0 y=1.01 l.wave=0.9
reflects=4
```
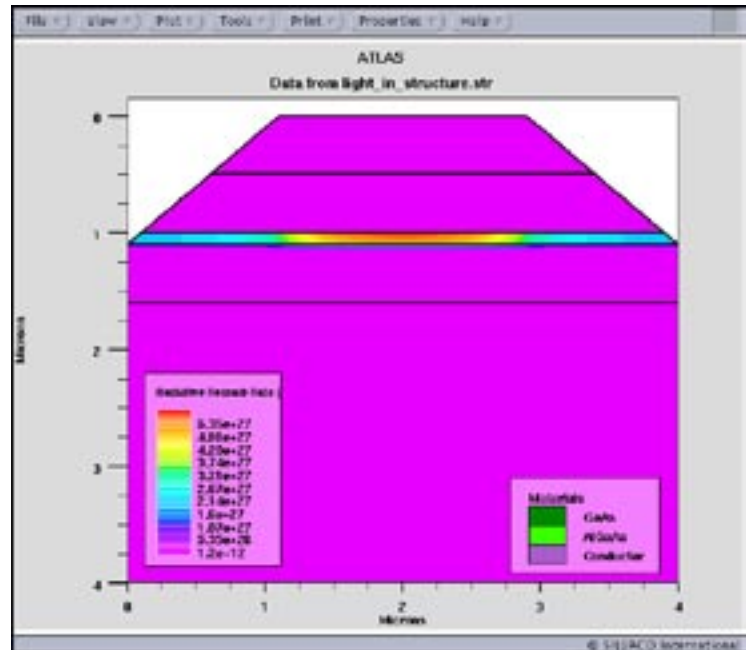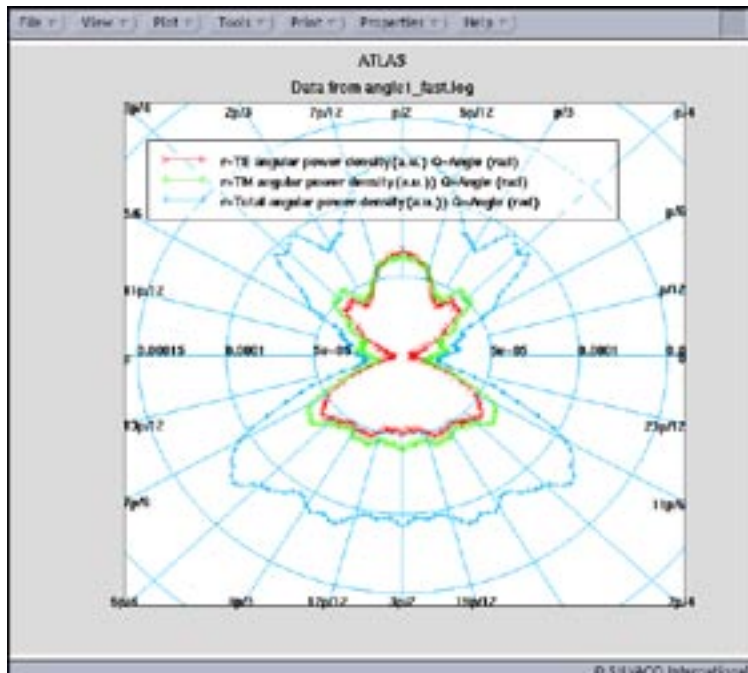

Figure 1. Simualted device.

Figure 2. TE and TM angular power distributions: no mirror.

where:

ANGPOWER specifies the name of the output file containing the angular power density versus output angle dependence obtained by reverse ray-tracing.

RAYPLOT specifies the name of the output file containing the information on each ray exciting the device in the process of reverse ray-tracing. This information includes relative ray power, polarization ratio, output angle, and initial angle at the origin (X,Y) of reverse ray-tracing. This file should be specified for the ray-tracing to proceed.

X, Y are the coordinates of the origin of the rays in the reverse ray-tracing. The origin should be located in the active region of the device.

L.WAVE is the wavelength of output radiation (needed for using appropriate refractive indexes of the materials). Should be specified for the ray-tracing to proceed.

In the above syntax readers will also notice the keyword fast. This is a new addition to the reverse ray tracing algorithm in Atlas that significantly increases the speed of the computation.

Figure 1 shows the simulated device with the photogeneration rate evident in the active region of the device. Figure 2 shows the transverse electrical and magnetic angular power density of the device as a function of angular distribution.

Using this method users may optimize their device structure for a more focussed beam. For example, users may wish to see what the effect of placing a mirror on the top of the device is on the angular distribution of the ray trace. The ray trace syntax would be written as:

```
save fast angpower=angle1_fast_
mirror.log rayplot=ray_angle1_
fast_mirror.log x=2.0 y=1.01
l.wave=0.9 mir.bottom numrays=360
reflects=4
```

where the effect of such a mirror is shown in Figure 3.

It is noted that the list of keywords related to the reverse ray trace is not exhaustive; a full list is given in the *ATLAS* manual.

A brief note on viewing the information in *TonyPlot*: In order to display the angular data a built in feature of *TonyPlot* is used, see Figure 4. To create such a plot as in Figure 2, firstly the respective file is loaded into *TonyPlot*, in this case the angpower file is used. Then within *TonyPlot*, plot...display is selected, which brings up the *TonyPlot*: Display (XY Graph) gui. Within the GUI there are several types of graphs that can be displayed; for the case of Figure 2 the polar type graph is selected by clicking on the respective symbol in the Type area of the GUI. After this type has been selected Convert Data is clicked. The *TonyPlot*: Display (XY Graph) gui now allows four polar graphs to be plotted which will be overlayed on each other to produce a graph as in Figure 2.
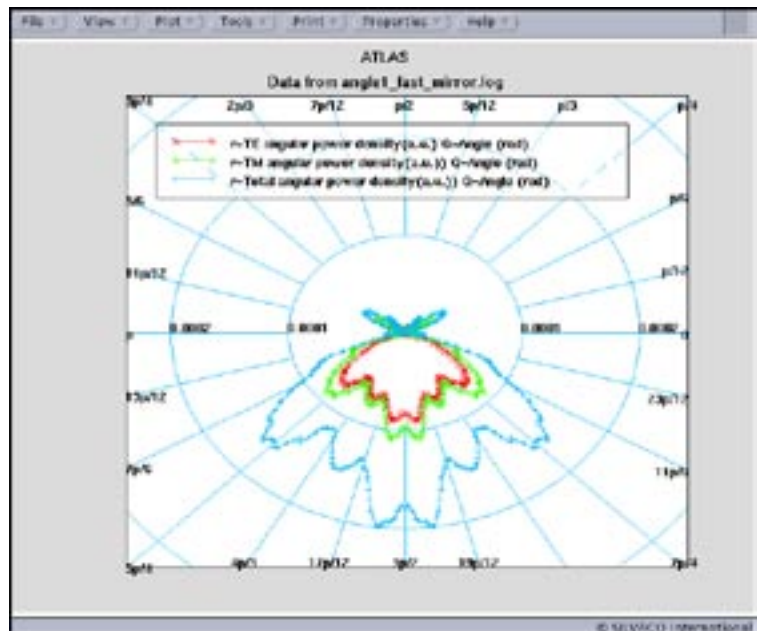

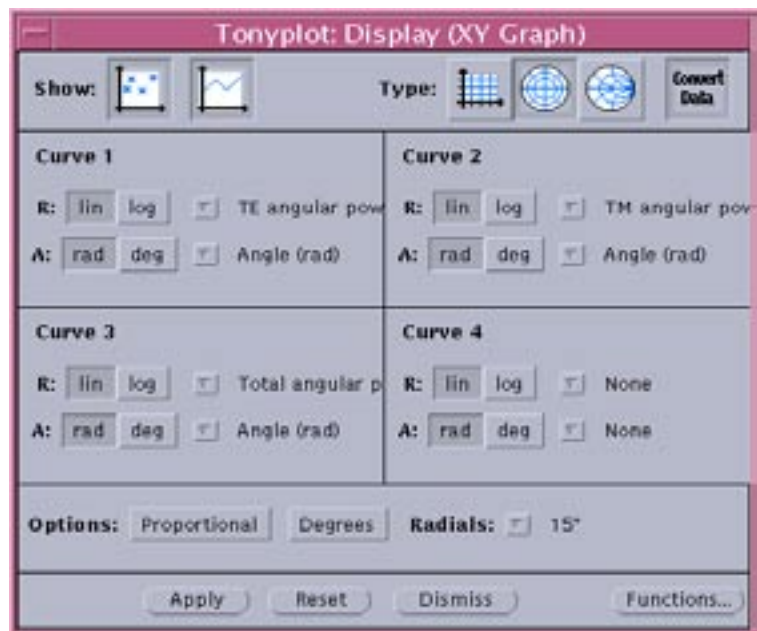Figure 3. TE and TM angular power distributions: with mirror.

Figure 4. *TonyPlot* display.

SILVACO
INTERNATIONAL

USA Headquarters:

Silvaco International
4701 Patrick Henry Drive, Bldg. 2
Santa Clara, CA 95054   USA

Phone: 408-567-1000
Fax: 408-496-6080

sales@silvaco.com
www.silvaco.com

Contacts:

Silvaco Japan
jpsales@silvaco.com

Silvaco Korea
krsales@silvaco.com

Silvaco Taiwan
twsales@silvaco.com

Silvaco Singapore
sgsales@silvaco.com

Silvaco UK
uksales@silvaco.com

Silvaco France
frsales@silvaco.com

Silvaco Germany
desales@silvaco.com

e*ECAD
PARTNER

*Products Licensed through Silvaco or e*ECAD*